

Atomic-scale visualization of defect-induced localized vibrations in GaN

Received: 20 April 2024

Accepted: 11 October 2024

Published online: 20 October 2024



Hailing Jiang¹, Tao Wang^{1,2}✉, Zhenyu Zhang¹, Fang Liu¹, Ruochen Shi^{2,3},
Bowen Sheng¹, Shanshan Sheng¹, Weikun Ge¹, Ping Wang¹, Bo Shen¹,
Bo Sun^{1,4}, Peng Gao^{2,3}, Lucas Lindsay⁵✉ & Xinqiang Wang¹✉

Phonon engineering is crucial for thermal management in GaN-based power devices, where phonon-defect interactions limit performance. However, detecting nanoscale phonon transport constrained by III-nitride defects is challenging due to limited spatial resolution. Here, we used advanced scanning transmission electron microscopy and electron energy loss spectroscopy to examine vibrational modes in a prismatic stacking fault in GaN. By comparing experimental results with *ab initio* calculations, we identified three types of defect-derived modes: localized defect modes, a confined bulk mode, and a fully extended mode. Additionally, the PSF exhibits a smaller phonon energy gap and lower acoustic sound speeds than defect-free GaN, suggesting reduced thermal conductivity. Our study elucidates the vibrational behavior of a GaN defect via advanced characterization methods and highlights properties that may affect thermal behavior.

III-Nitrides are important direct bandgap semiconductors commonly used in power electronic and optoelectronic devices^{1–11}. As the power density of modern III-Nitride based devices continues to increase, efficient thermal transfer has become critical to ensuring device reliability, prevention of overheating, and enhancement of device performance, especially as device sizes approach the nanoscale. In general, thermal transport in III-Nitride semiconductors is dominated by phonons, for which scattering resistance due to nano- and micro-scale structural defects can be significant. Since III-Nitride semiconductors are predominantly grown on substrates such as sapphire or silicon, a substantial lattice mismatch at the interface results in a high density of defects, which degrades the thermal conductivity and device performance^{12–19}. Therefore, rigorous understanding of phonon behaviors and transport in the presence of defects is critical for designing enhanced high-power-density III-Nitride based devices.

However, correlating phonon transport with defects is challenging, particularly for obtaining mode-resolved phonon information, for two primary reasons. First, most extended defects, such as grain

boundaries and dislocations, result in lattice strain and broken periodicity, which make correlation of specific defect atom vibrations with particular phonon modes difficult. With respect to simulation, poor periodicity also leads to oversized computational models and thus exaggerated numerical challenges. Second, localized defect vibrations can only be detected within a few nanometers of the defects, beyond the resolution of traditional measurement methods such as Raman scattering spectroscopy whose spatial resolution is constrained by laser wavelength.

To visualize defect-induced localized vibrations, here we focus on prismatic stacking fault (PSF) defects in GaN. PSF is a kind of stacking fault in (1120) crystallographic planes with a total displacement of $1/2[10\bar{1}1]$, as identified by Drum et al.²⁰ in AlN crystals, showing as 4 and 8 atom rings^{21,22}. It has twofold rotational symmetry along the [0001] direction and translational symmetry along $[10\bar{1}0]$ and $[0001]$ directions, which exhibits better periodicity than other planar defects. The central symmetry of PSF reduces delocalized dipole signals which typically ranges from 20 to 200 Å^{23,24}. It is known that dipole scattering

¹State Key Laboratory for Mesoscopic Physics and Frontiers Science Center for Nano-optoelectronics, School of Physics, Peking University, Beijing 100871, China. ²Electron Microscopy Laboratory, School of Physics, Peking University, Beijing 100871, China. ³International Center for Quantum Materials, School of Physics, Peking University, Beijing 100871, China. ⁴Tsinghua-Berkeley Shenzhen Institute, Tsinghua University, Shenzhen 518055, China. ⁵Materials Science and Technology Division, Oak Ridge National Laboratory, Oak Ridge, TN 37831, USA. ✉e-mail: cwwangtao@pku.edu.cn; lindsaylr@ornl.gov; wangshi@pku.edu.cn

is linked to the long-range Coulomb fields, which results from asymmetric stretching or deformation modes involving adjacent cations and anions^{25,26}. Therefore, the reduction of delocalized dipole signals weakens the long-range Coulomb fields and thus make it possible to achieve atomic resolution. In addition, PSFs are actually often detected in polar and non-polar GaN films^{27,28} or GaN crystals grown on needle-shaped GaN seeds obtained under high nitrogen pressure²⁹. They commonly occur at the junctions between two basal stacking faults (BSFs), forming closed domains or complex folded arrangements^{30–33}, indicating that BSFs can be terminated by PSFs^{27,34}. Therefore, it is important to study the vibrations of PSF since it is correlated with other planar defects as well.

In this study, we characterized vibrational modes of PSF in GaN using scanning transmission electron microscopy (STEM) and electron energy loss spectroscopy (EELS). STEM and EELS, equipped with a monochromator and spherical aberration correction, provide high spatial and energy resolution, enabling nanoscale measurement of phonon properties of different materials^{35–46} and localized phonon modes of defects^{47–53} and interfaces^{51–59}. Using these state-of-the-art tools, we are able to directly observe phonon energies and dispersions at defects and experimentally elucidate the influence of defects on phonon propagation. In both measurements and calculations, we identified three types of phonon modes around the PSFs: a localized defect mode (LDM), a confined bulk mode (CBM) and a fully extended mode (FEM). It is found that LDMs are attributed to vibration of atoms located at the center of the PSF. CBMs exist at atoms on both sides of the defect, but they are free of direct vibrational contributions from defect atoms, while FEMs are delocalized on all atoms over the entire system. In addition, phonon dispersion of bulk GaN was directly measured and compared with that of the PSF defect, demonstrating that the energy gap between acoustic (and folded acoustic-like modes) and high-frequency optic phonons in the PSF is smaller than that in defect-free GaN. This suggests that scattering of acoustic phonons by optic modes is more pronounced near the PSF than in bulk GaN^{60–62}, which will lead to increased thermal resistance in the defect zone.

Furthermore, the acoustic sound speeds extracted from the local PSF phonon dispersion is reduced compared with the bulk, which may lead to slower phonons and further enhanced thermal resistance in the defect zone^{63,64}. Our study builds a bridge between defect-phonon interactions and thermal conductivity in materials with high defect densities through direct observation of defect phonon modes.

Experimental setup

Figure 1a shows a schematic of the STEM-EELS used in our experiments. An electron beam is focused on the sample and an EELS aperture on the diffraction plane selectively collects scattered electrons with desired momentum transfers. The collected electrons are deflected by a magnetic prism and the vibrational signals of the sample are collected based on the loss of the electron beam kinetic energy. EELS is performed using a monochromated, aberration-corrected Nion U-HERMES200 STEM operating at an accelerating voltage of 60 kV. To maximize spatial resolution, a large beam convergence angle of 35 mrad and a collection angle of 25 mrad covering multiple Brillouin zones (BZs) are used (see illustration in Fig. 1b). The collected spectrum represents the local phonon density of states (DOS). To measure the phonon dispersion curves of the PSF in GaN, four-dimensional EELS (4D-EELS) was performed with a spatial resolution of ~ 2.4 nm and a momentum resolution of ~ 0.37 Å⁻¹ using a convergence angle of 3 mrad⁵⁴. We placed a slit aperture along the Γ -M- Γ direction on the diffraction plane (see depiction in Fig. 1c).

Results

A high-angle annular dark-field scanning transmission electron microscopy (HAADF-STEM) image of a PSF in GaN along the [0001] zone axis is shown in Fig. 1d. This defect often occurs when there is a deviation from the regular stacking sequence of atomic layers along specific crystallographic directions during the epitaxy of GaN. The surrounding area around the PSF is shown in Supplementary Figs. 1a–c. The PSF is a planar defect that extends into the [0001] zone axis with alternating 4-atom and 8-atom rings of Ga and N in the plane.

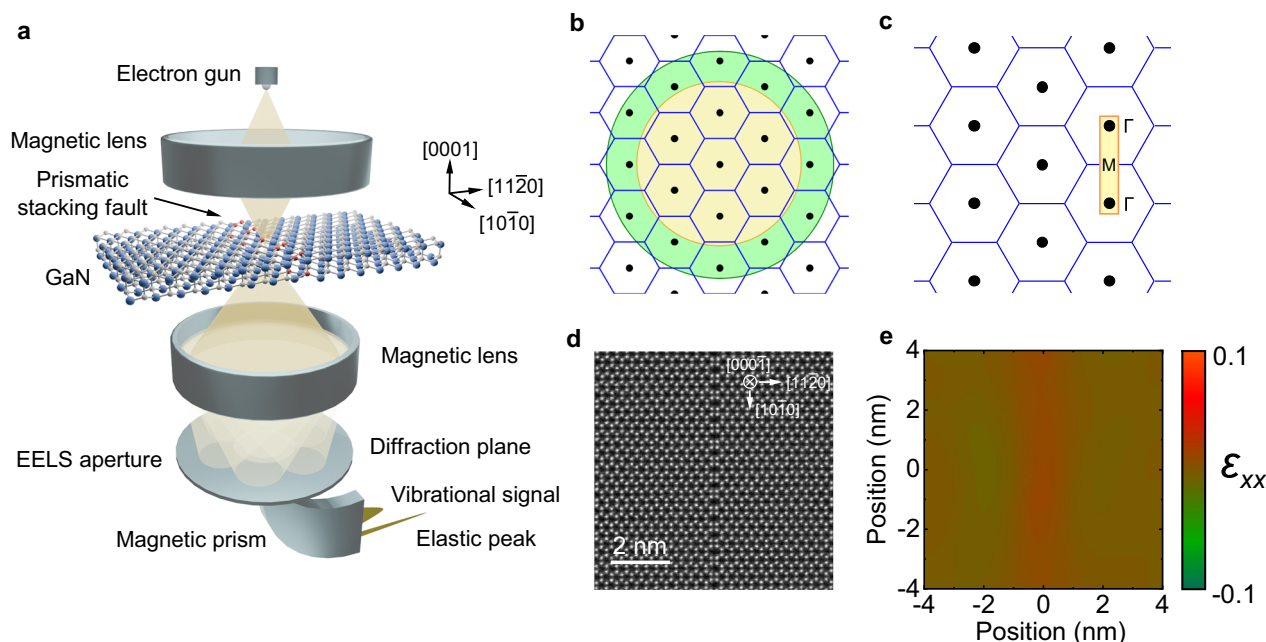


Fig. 1 | Experimental setup and PSF structure. **a** Schematic of the experimental setup for phonon measurements. The electron beam is focused on the GaN sample with a PSF. The energy loss of the electron beam is analysed using an EELS spectrometer to determine the vibrational energy of the sample. **b** Schematic of the EELS aperture placement in reciprocal space. The green circle marks the on-axis geometry of the aperture with a 35 mrad convergence semiangle, and the yellow

circle marks the position of the aperture with a 25 mrad collection semiangle. **c** Schematic of the experimental geometry, which shows the diffraction plane. The yellow rectangle illustrates the position of the slot aperture used in 4D-EELS. **d** HAADF-STEM image of the GaN PSF viewed along the [0001] zone axis. **e** GPA map of the PSF corresponding to the same area with (d), showing lattice strain component ϵ_{xx} .

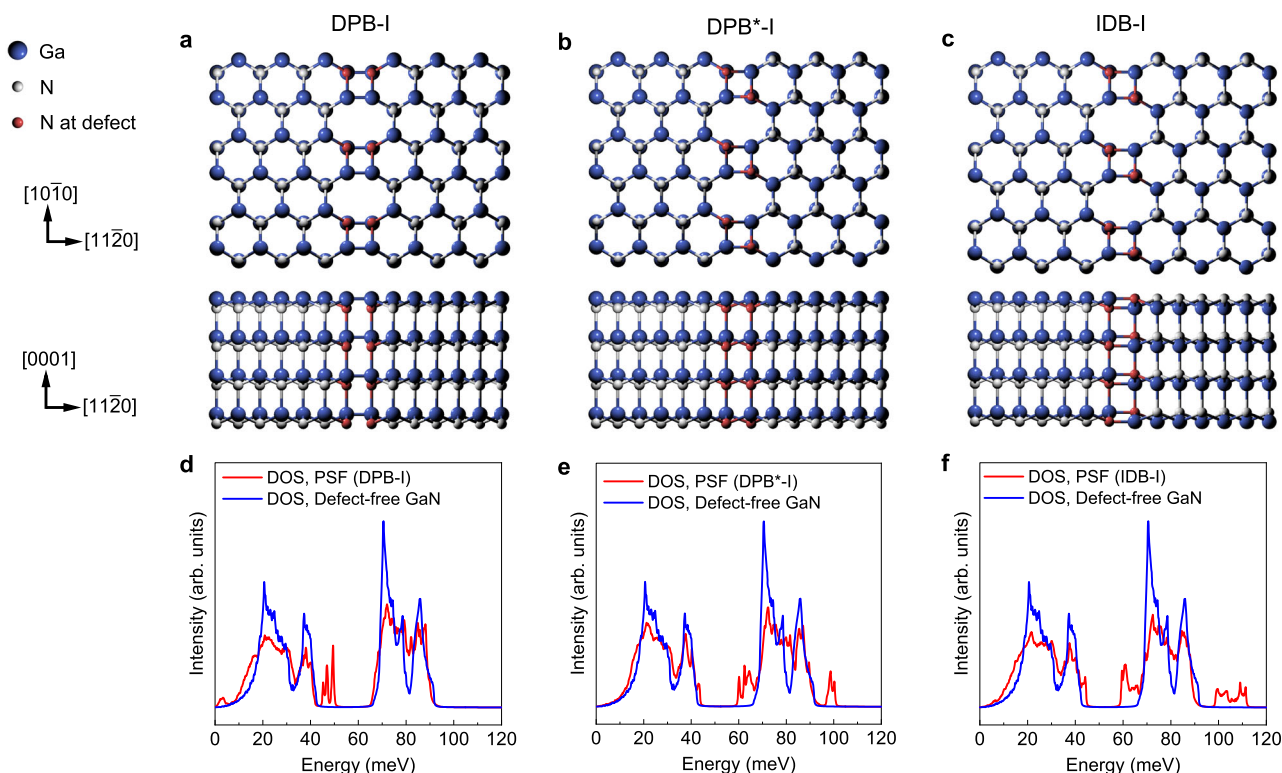


Fig. 2 | Three different PSF models and corresponding calculations. Atomistic schematics of (a) DPB-I, (b) DPB*-I, and (c) IDB-I viewed along the [0001] zone axis and the [10 $\bar{1}$ 0] zone axis. The calculated DOS were extracted from defect-free GaN (blue) and at the PSF (red) with atomic configurations of (d) DPB-I, (e) DPB*-I, and (f) IDB-I.

Geometric phase analysis (GPA) was performed on the HAADF-STEM image in Fig. 1d to investigate the defect-induced strain. The ε_{xx} , ε_{yy} , and ε_{xy} distortion components obtained from the GPA are given in Supplementary Figs. 2. Strains in all directions are less than 1% and the predominant strain is concentrated on the ε_{xx} component. Figure 1e shows the ε_{xx} distortion component of the PSF, which demonstrates that the strain is located at the center of the PSF with a range of approximately 1 nm, diminishing to become negligibly small in the bulk GaN beyond this.

Although the atomic structure of the PSF is clear in the HAADF-STEM image, three distinct atomic models (shown in Fig. 2a–c) can reproduce the same HAADF-STEM images seen by STEM along the [0001] zone axis. These PSF models include two kinds of double-position boundaries (DPB-I and DPB*-I) and an inversion domain boundary (IDB-I)²¹. DPB-I has a distinct stacking sequence with 1/2[10 $\bar{1}$ 0] horizontal shift across the boundary and contains seemingly unphysical Ga–Ga and N–N bonds at the boundary with the same bond length of 1.699 Å²¹. DPB*-I has an additional vertical displacement of 1/2[0001] and a total displacement of 1/2[10 $\bar{1}$ 1], forming Ga–N bonds at the boundary. IDB-I exhibits a total displacement of 1/2[10 $\bar{1}$ 0] with a lattice polarity inversion across the boundary and Ga–N bonds at the boundary. A previous theoretical study reported that the DPB-I has the highest domain wall energy of 246 meV/Å², slightly lower than the energy of the two free (11 $\bar{2}$ 0) surfaces (256 meV/Å²), indicating a metastable state²¹. The IDB-I has a calculated domain wall energy of 122 meV/Å², while the DPB*-I has the lowest energy with a value of 99 meV/Å²¹. This indicates that the DPB*-I should be the most stable and likely best representative of experiments. The existence of an N-vacancy can be ruled out, as the energy of DPB*-I with an N-vacancy at the 4-atom ring is 11.538 eV higher than that of the DPB*-I model. Then, we changed the zone axis to observe the atomic model of PSF in measurement. Since PSF contains a total displacement of 1/2[10 $\bar{1}$ 1], a 1/2[0001] translation vector is not visible on a [10 $\bar{1}$ 0] zone axis, and a 1/2[10 $\bar{1}$ 0] translation vector is not visible on a [0001] zone axis. The entire

displacement of PSF can only be detected along the [11 $\bar{2}$ 0] zone axis. The atomic models of DPB-I, DPB*-I, and IDB-I, as well as HAADF-STEM images from [11 $\bar{2}$ 0] zone axis, are shown in Supplementary Fig. 3. Since the PSF lies in the (11 $\bar{2}$ 0) plane, it cannot be seen edge on along the [11 $\bar{2}$ 0] zone axis. Therefore, the spatial resolution of the HAADF-STEM image is insufficient to make the N atoms visible. Nevertheless, the HAADF-STEM images showing semi-overlapping atomic structures with atoms projected in a hexagonal-like pattern^{22,27,30} match well with the DPB*-I atomic model, serving as supporting evidence.

From these atomic models, we determined the phonon dispersions and densities of states (DOSs) from first-principles calculations based on density functional theory (DFT) using the Quantum Espresso package⁶⁵ within the local density approximation (LDA). These were compared with those of bulk wurtzite GaN calculations just as done in ref. 60, which demonstrated excellent agreement with phonon frequencies obtained from inelastic X-ray scattering⁶⁶. PSF defect models were built into supercells (56 atoms) of the bulk GaN structure. Further details of the bulk calculations can be found in ref. 60 and for the defect structures in the Methods. Figure 2d–f show calculated DOSs of DPB-I, DPB*-I, and IDB-I compared with that of bulk GaN. The phonon DOS of bulk GaN exhibits four peaks at around 18–32 meV, 35–41 meV, 69–79 meV (attributed mostly to transverse optic (TO) modes), and 83–88 meV (attributed mostly to longitudinal optic (LO) modes). These peaks are also found in all three models, though with some broadening, demonstrating that the bulk like modes are captured in these supercells. Besides these bulk peaks, additional peaks occur in DPB-I around 45–50 meV, in DPB*-I around 60–65 and 95–100 meV, and in IDB-I around 60–65 and 98–111 meV, respectively. These additional vibrational peaks are attributed to defect modes originating from the PSF.

To support this, we show the measured atomically-resolved STEM-EEL spectra of the PSF (red) and defect-free GaN (blue) in Fig. 3a. The range, from which the EEL spectra of PSF and defect-free GaN are extracted, is shown in Supplementary Fig. 1d. The finite temperature

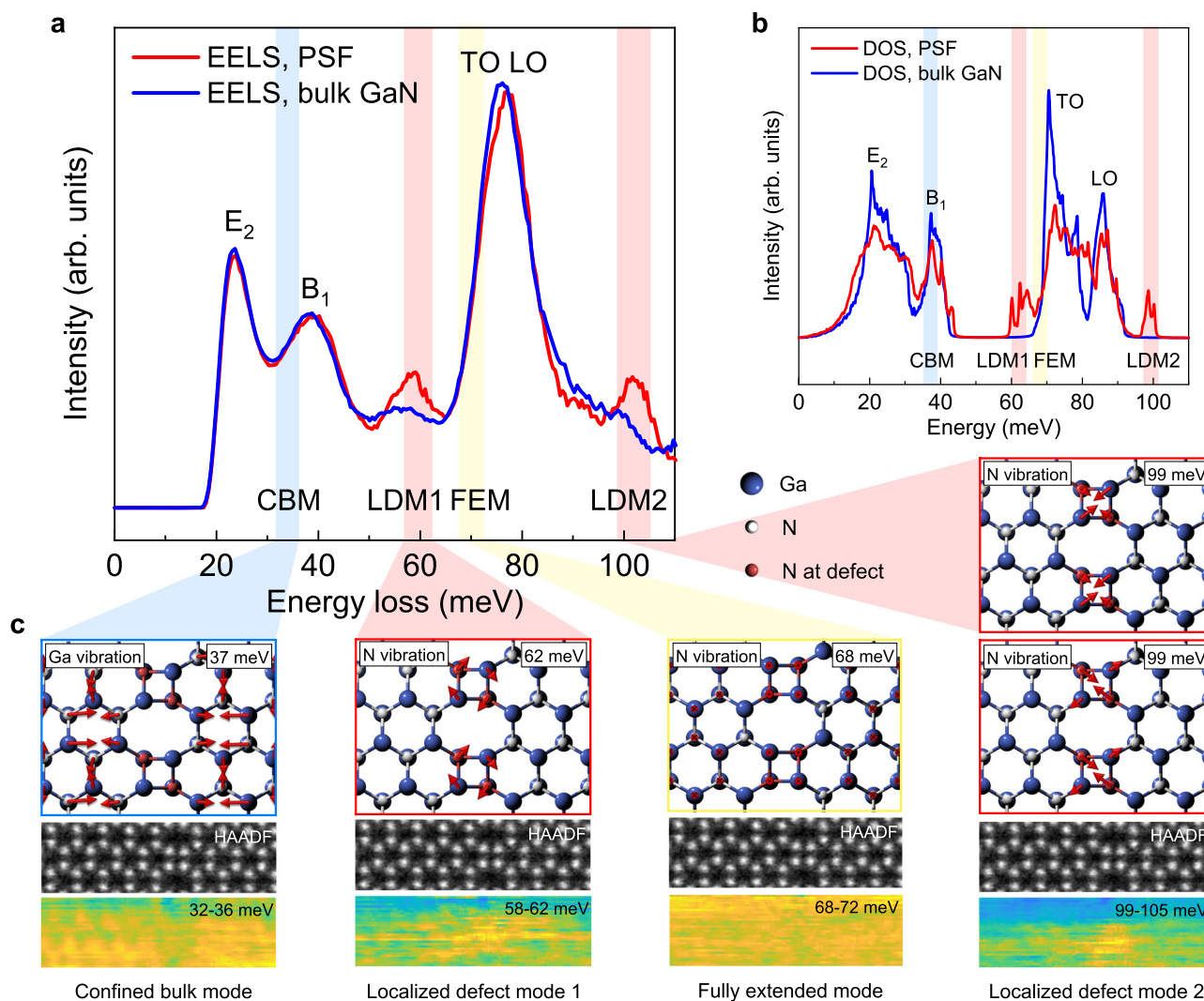


Fig. 3 | PSF on-axis EELS measurements and calculations. **a** EELS data extracted from the PSF (red) and bulk GaN (blue), the extracted range is shown in Supplementary Fig. 1d. **b** Calculated phonon spectra extracted from the PSF (red) and bulk GaN (blue). **c** Visualization of the atomic vibrations of two primary LDMs, a typical CBM and a typical FEM around the PSF. The upper figure shows the calculated vibrational eigenvectors. The arrows are the real parts of the eigenvectors showing a snapshot of the vibration amplitudes of the atoms. For FEM, the figure focuses on the main vibrations in the [0001] zone axis, overlooking the minor

vibrations within the plane. Details about vibrations in [0001] and [1010] zone axis are available in Supplementary Movies 1–10. The phonon energies around these calculated defect modes are shown in the red (LDM1 and LDM2), blue (CBM) and yellow (FEM) shaded regions of (b). The figures below are the corresponding experimental phonon intensity maps with the energy ranges shown in the red (LDM1 and LDM2), blue (CBM) and yellow (FEM) shaded regions of (a) and the HAADF-STEM images within the same areas.

effect on phonon frequencies comparing 0 K DFT calculations and room temperature measurement is expected to be less than 1 meV⁶⁷, and does not affect our conclusions. We note that the EELS signals of the defect-free GaN may be influenced by the PSF as the signals are extracted from an area ~1.5 nm from the PSF in the same measurement setup. There are three dominant EEL spectral peaks for defect-free GaN at 24, 39, and 77 meV. In comparison with the calculated DOS of defect-free GaN (see Fig. 2) and corresponding mode analysis, the two peaks at 24 and 39 meV correspond to acoustic phonon modes E₂ and B₁⁶⁸, respectively. The peak at 77 meV does not distinguish separate peaks for TO and LO phonons as seen in the calculations, likely due to the limited energy resolution of EELS measurements. Since the measurement is performed on-axis, the lack of resolution between the TO and LO peaks may also be a consequence of sampling surface phonon-polaritons that have energies between those of the TO and LO zone center phonons (Reststrahlen band)⁶⁹. In comparison with defect-free GaN, the EEL spectrum of the PSF reveals two additional peaks in the energy ranges of 53–64 meV and 97–106 meV. Comparing the

measured EELS spectrum with the calculated DOS of the three atomic models, the vibrational spectra of DPB*-I (Fig. 2e) best matches the experimental results. Additionally, to demonstrate that the calculated phonon spectrum of DPB*-I is not influenced by size effects due to PSF proximity in periodic supercell simulations, we calculated the DOS of a smaller model with 40 atoms, which reduces the normal GaN lattice on both sides of the PSF compared to that of the 56-atom DPB*-I model used here. As shown in Supplementary Fig. 4, the DOS for the two models of different sizes are remarkably similar, confirming that size effects are negligible for these structures. Therefore, from the phonon spectrum and the domain wall energy calculation discussed above, we conclude that the atomic structure of the GaN PSF is given by the DPB*-I model and restrict our further analysis to it.

Using the DPB*-I model (Figs. 2e, 3b), we now explore the origin of the phonon modes in the measured EEL spectra (Fig. 3a). Figure 3c shows calculated atomic vibrational eigenvectors for the DPB*-I supercell at energies of 37, 62, 68 and 99 meV corresponding with measured peaks in EELS intensity. HAADF-STEM images and phonon

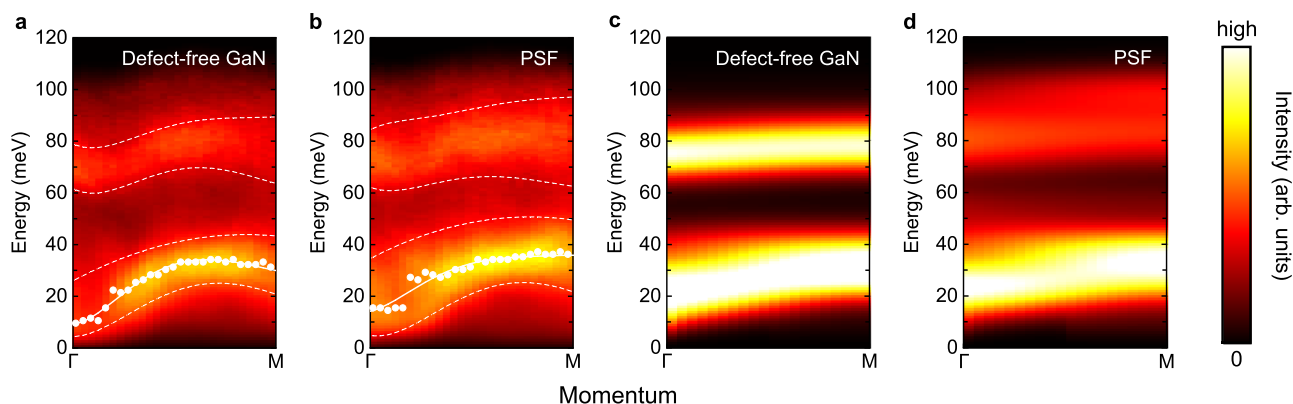


Fig. 4 | Experimental and simulated phonon dispersions at the GaN PSF.

Experimental phonon dispersion line profiles of (a) bulk GaN and (b) the GaN PSF defect, acquired with the slot aperture placed along the Γ -M- Γ line, which is shown in the yellow rectangle in Fig. 1c. The white dotted curves are eye guides for the approximate boundaries of the acoustic and optical phonon signals to show the energy gap. The white dots mark the points with the highest intensity at that

momentum and are fitted to a polynomial curve, whose slope gives a semi-quantitative representation of the average sound speed as the acoustic branches have the only appreciable dispersion in this frequency range near the zone center. The corresponding simulation results of (c) bulk GaN and (d) the PSF defect based on DFT calculations and scattering cross section.

intensity maps are also shown for these energy ranges. As demonstrated by the HAADF-STEM images and intensity maps, the peaks located at 58–62 and 99–105 meV are localized at the center 4-atom ring of the PSF and then rapidly decay within 0.75 nm, particularly for the higher frequency vibrations. These peaks are most likely correlated with localized defect phonon modes (LDM), which are labelled LDM1 and LDM2, respectively. From calculations, these LDMs are predominantly governed by the vibrations of N atoms in the 4-atom rings, while the other atoms remain largely stationary as shown in the corresponding calculated vibrational eigenvectors. LDM1 originates from vibrations of the 4-atom rings resembling a phonon vortex with rotational vibrational character around the center of the 4-atom rings. This vibrational eigenvector is similar to that previously found in asymmetric Si impurities in graphene⁷⁰. The lower energy of LDM1 is most likely due to the wide space between N atoms caused by their tangential vibrations. LDM2 encompasses two degenerate vibrational modes, where the N atoms in the 4-atom ring undergo vibrational motions towards each other. Conversely, the higher energy of LDM2 probably result from the close proximity of N atoms as they vibrate towards each other. We extracted the intensity attenuation of LDM1 and LDM2 as a function of distance from the defect core and determined their influence range. Supplementary Fig. 5 displays the integrated phonon intensities of LDM1 and LDM2 as a function of position. The stronger phonon intensity correlates with atoms in the HAADF-STEM image, showing the atomic spatial resolution of phonon detection. LDM1 and LDM2 are highly localized at the center of 4-atom ring, with full-widths at half maximum (FWHMs) of 0.93 nm and 0.50 nm, respectively. The larger FWHM of LDM1 compared to LDM2 may be attributed to that the energy range of LDM1 is close to the optical phonon energy of bulk GaN, resulting in the inclusion of a small number of bulk phonons. Therefore, the range of LDM2 may more accurately reflect the range of localized phonon modes. Furthermore, the measured EEL spectra extracted from the 8-atom ring are shown in Supplementary Fig. 6. LDM1 and LDM2 do not exist at the 8-atom ring as the vibrations occur on the 4-atom ring. The distinction observed in the EEL spectra between the 4-atom ring and the 8-atom ring highlights the exceptional spatial resolution achieved in our study. On the contrary, the other modes are delocalized as demonstrated by the broad smearing in their intensity maps. For the intensity peak in the 32–36 meV range where the EELS intensity map becomes weaker in the center of the PSF, we show the calculated eigenmotion of a typical vibrational mode in this energy range. This mode is confined to the bulk and is predominantly governed by the vibration of Ga atoms away

from the PSF while the atoms in the 4-atom ring remain static, which is called the confined bulk mode (CBM). In a sense, this mode is the inverse of the LDMs that were confined to the PSF. This mode is in the energy range of the bulk B1 mode, thus weakening of phonon intensity at the PSF in the EEL spectra is not significant; however, its confinement can be observed in the EELS intensity mapping. At the 8-atom ring, the weakening of phonon intensity in CBM is clear, as the vibration is away from this area. We note that the calculated behavior of this mode may be affected by the finite size of the supercells used. For the 68–72 meV energy range, a different mode type is typical, one that has eigenvibrations extended across the entire system, bulk and PSF, which is called the fully extended mode (FEM). This results in the experimental EELS intensity in the PSF region and the bulk GaN region being the same. The EELS intensity in the 8-atom ring is also the same as bulk GaN. Further visualizations and animations of the LDMs and above-described modes are given in the Supplementary Movies 1–10. As phonon-polaritons have energies between the TO and LO phonons (Reststrahlen band), none of the discussed modes exist within this range, except perhaps the FEM. Additionally, off-axis EELS measurements give similar results as the on-axis data (Supplementary Fig. 7), further supporting the conclusion that surface-phonon polaritons are not playing a significant role here.

Lastly, we explore the dependence of vibrational energy on momentum at the PSF with nanometer resolution using four-dimensional EELS (4D-EELS). We placed a slot from Γ to M (Γ M line) along the $[1120]$ direction (see details in Methods). Measured phonon dispersions with the beam located at defect-free GaN and the PSF are shown in Fig. 4a, b, respectively. The calculated EEL spectra based on DFT and the scattering cross-section⁵⁴ of bulk GaN and the DPB*-I supercell are shown in Fig. 4c, d for comparison. The calculated PSF supercell structure is orthorhombic rather than the hexagonal GaN structure. Although the limited EELS energy resolution prevents full mode quantification, the overall features show reasonable agreement with the calculated results. The energy range of experimental acoustic and optical phonons are guided for the eye by white dotted lines. It is noted that the energy range of the optical phonon dispersion increases at the PSF, contributing to the LDM1 and LDM2 observed in Fig. 3a and further confirming the existence of localized defect modes at the PSF, with an apparent rise in optical phonon energy. It is also shown that the energy gap between acoustic (and folded acoustic-like modes) and optical phonons at the PSF is smaller than that in defect-free GaN, which may enhance phonon-phonon scattering in this region⁶⁰. The estimated sound velocities of the PSF and defect-free GaN (slopes of

white lines in Fig. 4a, b; see details in Methods) demonstrate that the PSF sound speed is approximately 74% that of defect-free GaN (see details in Methods). This sound speed ratio is highly qualitative because it does not exclusively sample low frequency acoustic phonons, but also includes folded acoustic-like modes. The calculations also show an increase in acoustic phonon energy near the Γ point, while the slope near the Γ point decreases. More specifically, the sound speeds for the PSF are 3894 m/s (TA1), 4627 m/s (TA2), and 7034 m/s (LA), compared to those of GaN, which are 4188 m/s (TA1), 4424 m/s (TA2), and 7501 m/s (LA), giving a reduction for the PSF sound speed of 96.5%. The numerical discrepancy between the calculations (reduction to 96.5%) and experimental results (reduction to 74%) may be due to the calculations representing mode behaviors across the entire defect supercell structure, while the experiments focus specifically near the PSF. In addition, the intensity of acoustic phonons is stronger than that of optical phonons in both calculations and measurements. Both the smaller energy gap between acoustic and high frequency optical phonons and reduced phonon velocities should lead to decreased thermal conductivity in the region of the PSF. Although the impact of defects on the reduction of macroscopic thermal conductivity is dependent on defect density^{47–19}, disordered interfaces are expected to facilitate more energy transfer through increased mode-mixing as they relax momentum conservation rules, acting as phonon bridges from one material to the other⁵⁸, and leading to reduced interfacial resistance. PSFs have higher symmetry with clean interfaces that preserve phonon momentum conservation conditions that lead to less bridging and thus greater thermal resistivity than defects with atomic-level disorder.

Discussion

In summary, defect phonon modes around a PSF in GaN were visualized through STEM-EELS. By comparing the EELS data with DFT-derived phonon DOSs of three possible PSF models (DPB-I, DPB*-I and IDB-I) and calculated energetics, we conclude that the atomic structure of the PSF is DPB*-I. Through comparison of experimental and theoretical results, three types of PSF-associated modes are uncovered: those confined to the PSF (LDMs), those confined to the bulk (CBMs), and those extended over both (FEMs). Furthermore, we measured the phonon dispersions near and at the PSF using 4D-EELS. The energy gap between the acoustic (and folded acoustic-like modes) and optical branches is reduced in the PSF, which is caused by an LDM, indicating the possibility of enhanced phonon-phonon scattering over that in bulk GaN. Additionally, the average sound speed, determined semi-quantitatively from measurement fits, in the PSF is reduced to approximately 74% of that in defect-free GaN, and supported by DFT calculations. We conjecture that the phonon behaviors detected here may be applicable to similar extended defects such as edge dislocations. No previous experimental detection of the phonon modes only extended on one side of defect exist, which is similar to the partially extended modes at the interface between boron nitride and diamond⁵⁴. This is due to the high symmetry present on both sides of PSF, in contrast to interfaces between two different materials. Further exploration is necessary to detect symmetry breaking defects, which often exhibit strong strain fields and are difficult to visualize. Overall, our study gives mode-resolved microscopic details regarding phonon behaviors near extended defects, providing valuable insights into defect engineering for targeted phonon-derived applications such as thermal management.

Methods

Sample preparation and characterization

Wurtzite quasi-van der Waals epitaxial (vdWe) GaN films were grown on a graphene/sapphire substrate using plasma-assisted molecular beam epitaxy (MBE). The in situ RHEED image of GaN films is shown in Supplementary Fig. 8. The streaky RHEED patterns indicate a flat

surface, where no nitrogen reconstruction can be detected. As the growth progresses, nucleation islands coalesce and eventually form a GaN film consisting of a prismatic stacking fault (PSF) defect. A transmission electron microscopy (TEM) lamella was cut by a Thermo Fisher Scientific Helios G4 UX focused ion beam (FIB) system. To determine the atomic arrangement of the GaN planar defect, scanning transmission electron microscopy (STEM) measurements were performed using a spherical aberration-corrected FEI Titan Cubed Themis G2 300.

Electron energy loss spectroscopy (EELS) data acquisition

STEM-EELS measurements were performed using a Nion HERMES 200 microscope operating at 60 kV at room temperature equipped with both a monochromator and an aberration corrector. 3D-EELS datasets were obtained with a convergence semiangle of 35 mrad and a collection semiangle of 25 mrad. The STEM-EELS on-axis dataset was acquired in a 100×30 pixels mapping area covering a region of 3×0.9 nm that included the PSF. The dwell time for each pixel was set to 200 ms, resulting in a total acquisition time of approximately 10 minutes for each dataset. The sample drift during the acquisition was typically less than 1 nm. The energy resolution achieved under these conditions was approximately 10 meV, while the spatial resolution was approximately 0.2 nm.

For the acquisition of the 4D-EELS datasets, a convergence semiangle of 3 mrad was used, and a slot aperture with an aspect ratio of 16:1 was placed along the Γ -M- Γ direction. To increase the signal-to-background ratio and avoid strong central diffraction spots, the slot aperture was displaced away from the central Γ point. The typical dwell time per pixel was set to 15 s, resulting in a total acquisition time of approximately 32 minutes for each dataset. The energy resolution achieved under these conditions was approximately 15 meV.

Ab initio calculations

Density functional theory (DFT) calculations for the bulk and defect systems were performed with the Quantum Espresso package⁶⁵ within the local density approximation (LDA). The calculated bulk wurtzite structural parameters ($a = 3.164$ Å, $c = 5.150$ Å, and $u = 0.377$) and phonon frequencies were determined exactly as in ref. 60. These give good agreement with measured phonon frequencies from inelastic x-ray scattering⁶⁶.

Model interfacial PSF structures (see Fig. 2) were built using the bulk lattice parameters in 56-atom orthorhombic unit cells that consisted of the PSF structure (16 atoms) and two bulk hexagonal ring structures on either side of the interface (20 atoms each). Variations between the different model arrangements were described above. The use of periodic boundary conditions (as in typical DFT calculations) with this unit cell gives periodic PSF interfaces with an 11.32 Å centre-to-centre distance between them. This provides enough space to nearly recover the bulk vibrational behaviour for atoms sandwiched between the two interfaces. From these 56-atom unit cells, $3 \times 1 \times 2$ supercells (336 atoms) were built (in-plane parallel to the interface \times in-plane perpendicular to the interface \times cross-plane parallel to the interface) to avoid spurious periodic forces in the DFT simulations.

Harmonic interatomic force constants (hIFCs) were constructed by finite difference methods for numerical differentiation of the interatomic forces⁷¹. These forces were determined from DFT electronic structure calculations of various supercell images, each with a strategically displaced unit cell atom (0.05 Å from equilibrium) along different Cartesian directions. Given the hIFCs, the phonon frequencies ($\omega_{\mathbf{q}j}$) and eigenvectors ($\mathbf{e}_{\mathbf{q}jk}$) were determined via diagonalization of the dynamical matrices for a given wavevector (\mathbf{q}), where j represents the phonon polarization (168 in total) and k represents the atom⁷². Note that long-range Coulomb corrections were not explicitly included for the defect dynamical matrices. Nonetheless, the Ga and N vibrations away from the interface exhibited similar behaviour as that in the bulk calculations with

polar corrections. The vibrational density of states ($\text{DOS}(\omega)$) and atom-projected $\text{DOS}(\omega, k)$ were obtained via:

$$\text{DOS}(\omega) = \sum_k \text{DOS}(\omega, k) = \sum_{\mathbf{q}, jk} \left| \epsilon_{\mathbf{q}, jk} \right|^2 \delta(\omega - \omega_{\mathbf{q}, j}) \quad (1)$$

where the wavevector sum is over the first Brillouin zone and the energy delta function is approximated by a Lorentzian of smearing width 0.15 meV.

The 4D-EELS DFPT calculation was conducted using Quantum ESPRESSO, employing the local density approximation and norm-conserving pseudopotentials. For wavefunctions, the kinetic energy cutoff was set to 44 Rydbergs (Ry), while charge density and potential cutoff was 395 Ry. The scattering cross section is represented as^{40,42,73}:

$$\frac{d^2\sigma}{d\omega d\Omega} \propto \sum_{\mathbf{q}, j} \left| F_{\mathbf{q}, j} \right|^2 \left[\frac{n_{\mathbf{q}, j} + 1}{\omega_{\mathbf{q}, j}(\mathbf{q})} \delta(\omega - \omega_{\mathbf{q}, j}) + \frac{n_{\mathbf{q}, j}}{\omega_{\mathbf{q}, j}} \delta(\omega + \omega_{\mathbf{q}, j}) \right] \quad (2)$$

where $n_{\mathbf{q}, j}$ is the phonon occupancy number. The Dirac delta function is represented by $\delta(x)$. The coupling factor is given by:

$$F_{\mathbf{q}, j} \propto \frac{1}{q^2} \sum_k \frac{1}{\sqrt{M_k}} e^{-i\mathbf{q} \cdot \mathbf{r}_k} e^{-W_{\mathbf{q}, k}} Z_{\mathbf{q}, k} \left[\epsilon_{\mathbf{q}, jk} \cdot \mathbf{q} \right] \quad (3)$$

where M_k is the mass of atom k , $Z_{\mathbf{q}, k}$ is the effective charge, \mathbf{r}_k is the real-space position, and $e^{-2W_{\mathbf{q}, k}(\mathbf{q})}$ is the Debye-Waller factor⁷⁴. $Z_{\mathbf{q}, k}$ was calculated as per literature⁷³, with atomic form factors constructed from parameters in the literature⁷⁵.

EELS data processing

For each 3D-EELS dataset, the EEL spectra were initially aligned using normalized cross-correlation to correct for beam energy drift. Then, the spectra were normalized by the zero-loss peak (ZLP) total intensity. To eliminate Gaussian noise, a block-matching and 3D filtering algorithm was applied^{76,77}. The EELS background was fitted using a Pearson function²⁵ and subtracted. To enhance the resolution and reduce the broadening effect caused by finite energy resolution, Lucy-Richardson deconvolution was employed. The statistical factors of the background-subtracted spectra were further corrected, which resulted from the different scattering probability of phonons with different frequencies⁷⁸, to make it more comparable to the real phonon DOS.

For each 4D-EELS dataset, EEL spectra were first registered by their normalized cross correlation to correct possible beam energy drift and momentum distortion. After the alignment, we applied block-matching and 3D filtering (BM3D) algorithm to remove Gaussian noise^{76,77}. For each momentum and each energy channel, the data is denoised in two spatial dimensions, where the noise level is individually estimated based on high-frequency elements in the Fourier domain. To enhance the resolution and reduce the broadening effect caused by finite energy resolution, Lucy-Richardson deconvolution was employed. The white dots in Fig. 4a, b highlight the points with the highest intensity of acoustic phonons at their respective momentum values, and these dots are then fitted with a polynomial curve for visualization. We obtain the sound speed ratio between PSF and GaN by averaging the slope ratios for the two systems on 6 different momentum ranges from $\Gamma \sim 0.3\text{M}$ to $\Gamma \sim 0.5\text{M}$.

Data availability

The data that support the findings of this study are available from the corresponding author upon request.

Code availability

The codes that support the findings of this study are available from the corresponding author upon request.

References

- Simon, J., Protasenko, V., Lian, C., Xing, H. & Jena, D. Polarization-induced hole doping in wide-band-gap uniaxial semiconductor heterostructures. *Science* **327**, 60–64 (2010).
- Yan, R. et al. GaN/NbN epitaxial semiconductor/superconductor heterostructures. *Nature* **555**, 183–189 (2018).
- Chaudhuri, R. et al. A polarization-induced 2D hole gas in undoped gallium nitride quantum wells. *Science* **365**, 1454–1457 (2019).
- Parker, M. A gallium nitride HEMT that enhances. *Nat. Electron.* **4**, 858 (2021).
- Kuykendall, T., Ulrich, P., Aloni, S. & Yang, P. Complete composition tunability of InGaN nanowires using a combinatorial approach. *Nat. Mater.* **6**, 951–956 (2007).
- Morkoç, H. & Mohammad, S. N. High-luminosity blue and blue-green gallium nitride light-emitting diodes. *Science* **267**, 51–55 (1995).
- Someya, T. et al. Room temperature lasing at blue wavelengths in gallium nitride microcavities. *Science* **285**, 1905–1906 (1999).
- Mohanty, S. K., Chen, Y. Y., Yeh, P. H. & Horng, R. H. Thermal management of GaN-on-Si high electron mobility transistor by copper filled micro-trench structure. *Sci. Rep.* **9**, 19691 (2019).
- Li, D. et al. Deep-ultraviolet micro-LEDs exhibiting high output power and high modulation bandwidth simultaneously. *Adv. Mater.* **34**, 2109765 (2022).
- Rong, X. et al. High-output-power ultraviolet light source from quasi-2D GaN quantum structure. *Adv. Mater.* **28**, 7978–7983 (2016).
- Liu, S. et al. Drive high power UVC-LED wafer into low-cost 4-inch era: effect of strain modulation. *Adv. Funct. Mater.* **32**, 2112111 (2022).
- Wang, T., Carrete, J., Mingo, N. & Madsen, G. K. H. Phonon scattering by dislocations in GaN. *ACS Appl. Mater. Interfaces* **11**, 8175–8181 (2019).
- Ma, J., Wang, X., Huang, B. & Luo, X. Effects of point defects and dislocations on spectral phonon transport properties of wurtzite GaN. *J. Appl. Phys.* **114**, 074311 (2013).
- Termentzidis, K. et al. Impact of screw and edge dislocations on the thermal conductivity of individual nanowires and bulk GaN: a molecular dynamics study. *Phys. Chem. Chem. Phys.* **20**, 5159–5172 (2018).
- Katcho, N. A., Carrete, J., Li, W. & Mingo, N. Effect of nitrogen and vacancy defects on the thermal conductivity of diamond: an ab initio Green's function approach. *Phys. Rev. B* **90**, 094117 (2014).
- Scott, E. A. et al. Phonon scattering effects from point and extended defects on thermal conductivity studied via ion irradiation of crystals with self-impurities. *Phys. Rev. Mater.* **2**, 095001 (2018).
- Li, H. et al. GaN thermal transport limited by the interplay of dislocations and size effects. *Phys. Rev. B* **102**, 014313 (2020).
- Sun, B. et al. Dislocation-induced thermal transport anisotropy in single-crystal group-III nitride films. *Nat. Mater.* **18**, 136–140 (2019).
- Kotchetkov, D., Zou, J., Balandin, A. A., Florescu, D. I. & Pollak, F. H. Effect of dislocations on thermal conductivity of GaN layers. *Appl. Phys. Lett.* **79**, 4316–4318 (2001).
- Drum, C. Intersecting faults on basal and prismatic planes in aluminium nitride. *Philos. Mag.* **11**, 313–334 (1965).
- Elsner, J. et al. Domain boundaries on {1120} planes in GaN: a theoretical study. *Phys. Rev. B* **58**, 15347–15350 (1998).
- Vermaut, P., Nouet, G. & Ruterana, P. Observation of two atomic configurations for the {1210} stacking fault in wurtzite (Ga, Al) nitrides. *Appl. Phys. Lett.* **74**, 694–696 (1999).
- Crozier, P. Vibrational and valence aloof beam EELS: a potential tool for nondestructive characterization of nanoparticle surfaces. *Ultramicroscopy* **180**, 104–114 (2017).
- Venkatraman, K., Rez, P., March, K. & Crozier, P. The influence of surfaces and interfaces on high spatial resolution vibrational EELS from SiO₂. *Microscopy* **67**, i14–i23 (2018).
- Venkatraman, K., Levin, B., March, K., Rez, P. & Crozier, P. Vibrational spectroscopy at atomic resolution with electron impact scattering. *Nat. Phys.* **15**, 1237–1241 (2019).

26. Ibach, H. & Mills, L. *Electron Energy Loss Spectroscopy and Surface Vibrations* (Academic Press, 1982).
27. Zakharov, D. et al. Structural TEM study of nonpolar a-plane gallium nitride grown on (1120) 4H-SiC by organometallic vapor phase epitaxy. *Phys. Rev. B* **71**, 235334 (2005).
28. Hu, Y., Kramer, S., Fini, P. & Speck, J. Atomic structure of prismatic stacking faults in nonpolar a-plane GaN epitaxial layers. *Appl. Phys. Lett.* **101**, 112102 (2012).
29. Smalc-Koziorowska, J. et al. Structural defects in GaN crystals grown by HVPE on needle-shaped GaN seeds obtained under high N₂ pressure. *J. Cryst. Growth* **311**, 1407–1410 (2009).
30. Vermaut, P., Ruterana, P., Nouet, G., Salvador, A. & Morkoc, H. Prismatic defects in GaN grown on 6H-SiC by molecular beam epitaxy. *Mater. Sci. Eng. B* **43**, 279–282 (1997).
31. Massabuau, F. et al. Morphological, structural, and emission characterization of trench defects in InGaN/GaN quantum well structures. *Appl. Phys. Lett.* **101**, 212107 (2012).
32. Bai, J. et al. Structural defects and luminescence features in heteroepitaxial GaN grown on on-axis and misoriented substrates. *J. Appl. Phys.* **97**, 116101 (2005).
33. Smalc-Koziorowska, J. et al. The heterogeneous nucleation of threading dislocations on partial dislocations in III-nitride epilayers. *Sci. Rep.* **10**, 17371 (2020).
34. Ruterana, P. et al. Formation mechanism and relative stability of the {1120} stacking fault atomic configurations in wurtzite (Al,Ga,In) nitrides. *Phys. Rev. B* **59**, 15917–15925 (1999).
35. Zhang, Z. et al. Probing hyperbolic shear polaritons in β -Ga₂O₃ nanostructures using STEM-EELS. *Adv. Mater.* **36**, 2204884 (2024).
36. Govyadinov, A. A. et al. Probing low-energy hyperbolic polaritons in van der Waals crystals with an electron microscope. *Nat. Commun.* **8**, 95 (2017).
37. Idrobo, J. C. et al. Temperature measurement by a nanoscale electron probe using energy gain and loss spectroscopy. *Phys. Rev. Lett.* **120**, 095901 (2018).
38. Li, N. et al. Direct observation of highly confined phonon polaritons in suspended monolayer hexagonal boron nitride. *Nat. Mater.* **20**, 43–48 (2021).
39. Konečná, A., Li, J., Edgar, J. H., García de Abajo, F. J. & Hachtel, J. A. Revealing nanoscale confinement effects on hyperbolic phonon polaritons with an electron beam. *Small* **17**, 2103404 (2021).
40. Lagos, M. J., Trügler, A., Hohenester, U. & Batson, P. E. Mapping vibrational surface and bulk modes in a single nanocube. *Nature* **543**, 529–532 (2017).
41. Li, X. et al. Three-dimensional vectorial imaging of surface phonon polaritons. *Science* **371**, 1364–1367 (2021).
42. Senga, R. et al. Position and momentum mapping of vibrations in graphene nanostructures. *Nature* **573**, 247–250 (2019).
43. Li, Y., Qi, R., Shi, R., Li, N. & Gao, P. Manipulation of surface phonon polaritons in SiC nanorods. *Sci. Bull.* **65**, 820–826 (2020).
44. Jokisaari, J. R. et al. Vibrational spectroscopy of water with high spatial resolution. *Adv. Mater.* **30**, 1802702 (2018).
45. Lagos, M. J. & Batson, P. E. Thermometry with subnanometer resolution in the electron microscope using the principle of detailed balancing. *Nano Lett.* **18**, 4556–4563 (2018).
46. Qi, R. et al. Four-dimensional vibrational spectroscopy for nanoscale mapping of phonon dispersion in BN nanotubes. *Nat. Commun.* **12**, 1179 (2021).
47. Yan, X. et al. Single-defect phonons imaged by electron microscopy. *Nature* **589**, 65–69 (2021).
48. Senga, R. et al. Imaging of isotope diffusion using atomic-scale vibrational spectroscopy. *Nature* **603**, 68–72 (2022).
49. Hage, F. S., Radtke, G., Kepaptsoglou, D. M., Lazzeri, M. & Ramasse, Q. M. Single-atom vibrational spectroscopy in the scanning transmission electron microscope. *Science* **367**, 1124–1127 (2020).
50. Xu, M. et al. Single-atom vibrational spectroscopy with chemical-bonding sensitivity. *Nat. Mater.* **22**, 612–618 (2023).
51. Haas, B. et al. Atomic-resolution mapping of localized phonon modes at grain boundaries. *Nano Lett.* **23**, 5975–5980 (2023).
52. Hoglund, E. R. et al. Direct visualization of localized vibrations at complex grain boundaries. *Adv. Mater.* **35**, 2208920 (2023).
53. Yan, J. et al. Nanoscale Localized Phonons at Al₂O₃ Grain Boundaries. *Nano Lett.* **24**, 3323–3330 (2024).
54. Qi, R. et al. Measuring phonon dispersion at an interface. *Nature* **599**, 399–403 (2021).
55. Wu, M. et al. Effects of localized interface phonons on heat conductivity in ingredient heterogeneous solids. *Chin. Phys. Lett.* **40**, 036801 (2023).
56. Gadre, C. A. et al. Nanoscale imaging of phonon dynamics by electron microscopy. *Nature* **606**, 292–297 (2022).
57. Hoglund, E. R. et al. Emergent interface vibrational structure of oxide superlattices. *Nature* **601**, 556–561 (2022).
58. Li, Y. H. et al. Atomic-scale probing of heterointerface phonon bridges in nitride semiconductor. *Proc. Natl. Acad. Sci. USA* **119**, e2117027119 (2022).
59. Cheng, Z. et al. Experimental observation of localized interfacial phonon modes. *Nat. Commun.* **12**, 6901 (2021).
60. Lindsay, L., Broido, D. A. & Reinecke, T. L. Thermal conductivity and large isotope effect in GaN from first principles. *Phys. Rev. Lett.* **109**, 095901 (2012).
61. Lindsay, L. & Broido, D. A. Three-phonon phase space and lattice thermal conductivity in semiconductors. *J. Phys. Condens. Matter* **20**, 165209 (2008).
62. Lindsay, L., Broido, D. A. & Reinecke, T. L. First-principles determination of ultrahigh thermal conductivity of boron arsenide: a competitor for diamond? *Phys. Rev. Lett.* **111**, 025901 (2013).
63. Li, M. et al. Nonperturbative quantum nature of the dislocation-phonon interaction. *Nano Lett.* **17**, 1587–1594 (2017).
64. Hanus, R. et al. Thermal transport in defective and disordered materials. *Appl. Phys. Rev.* **8**, 031311 (2021).
65. Giannozzi, P. et al. QUANTUM ESPRESSO: a modular and open-source software project for quantum simulations of materials. *J. Phys. Condens. Matter* **21**, 395502 (2009).
66. Ruf, T. et al. Phonon dispersion curves in wurtzite-structure GaN determined by inelastic x-ray scattering. *Phys. Rev. Lett.* **86**, 906–909 (2001).
67. Wei, B. et al. High-order phonon anharmonicity and thermal conductivity in GaN. *Phys. Rev. B* **109**, 155204 (2024).
68. Davydov, V. et al. Phonon dispersion and Raman scattering in hexagonal GaN and AlN. *Phys. Rev. B* **58**, 12899–12907 (1998).
69. Caldwell, J. et al. Low-loss, infrared and terahertz nanophotonics using surface phonon polaritons. *Nanophotonics* **4**, 44–68 (2015).
70. Bao, D. L. et al. Phonon vortices at heavy impurities in two-dimensional materials. *Nanoscale Horiz.* **9**, 248–253 (2024).
71. Lindsay, L. & Polanco, C. A. Thermal transport by first-principles anharmonic lattice dynamics. In: *Handbook of Materials Modeling* 735–765 (Springer, Cham, Switzerland, 2020).
72. Ziman, J. M. *Electrons and Phonons* (Oxford University Press, Oxford, United Kingdom, 1960).
73. Nicholls, R. J. et al. Theory of momentum-resolved phonon spectroscopy in the electron microscope. *Phys. Rev. B* **99**, 094105 (2019).
74. Vila, F. D., Rehr, J. J., Rossner, H. H. & Krappe, H. J. Theoretical X-ray absorption Debye-Waller factors. *Phys. Rev. B* **76**, 014301 (2007).
75. Waasmaier, D. & Kirfel, A. New analytical scattering-factor functions for free atoms and ions. *Acta Crystallogr. A* **51**, 416–431 (1995).
76. Zhou, J. et al. Observing crystal nucleation in four dimensions using atomic electron tomography. *Nature* **570**, 500–503 (2019).

77. Dabov, K., Foi, A., Katkovnik, V. & Egiazarian, K. Image denoising by sparse 3-D transform-domain collaborative filtering. *IEEE Trans. Image Process.* **16**, 2080–2095 (2007).
78. Batson, P. E. & Lagos, M. J. Interpretation of meV resolution phonon EELS data. *Microsc. Microanal.* **24**, 412–413 (2018).

Acknowledgements

This work was supported by the National Key R&D Program of China (No. 2022YFA1206700) (W.T.), the Beijing Natural Science Foundation (No. Z2000004) (W.X.), the Guangdong Major Project of Basic and Applied Basic Research (2023B0303000012) (W.X.), the National Natural Science Foundation of China (No. 62321004, 62104010, and 62227817) (W.X.), and the National Natural Science Foundation of China (No. 62374010) (W.T.). This work was supported by the High-performance Computing Platform of Peking University. We acknowledge the Electron Microscopy Laboratory of Peking University for the use of electron microscopes. Calculations and manuscript development (L.L.) were supported by the U.S. Department of Energy, Office of Science, Office of Basic Energy Sciences, Material Sciences and Engineering Division. The calculations used resources of the Compute and Data Environment for Science (CADES) at the Oak Ridge National Laboratory, which is supported by the Office of Science of the U.S. Department of Energy under Contract No. DE-AC05-00OR22725, and resources of the National Energy Research Scientific Computing Center, which is supported by the Office of Science of the U.S. Department of Energy under Contract No. DE-AC02-05CH11231.

Author contributions

T. Wang and X.Q. Wang conceived and supervised the project; H.L. Jiang performed the STEM-EELS experiment and data analysis assisted by Z.Y. Zhang and R.C. Shi with the guidance of X.Q. Wang and T. Wang; L.R. Lindsay performed DFT calculations; R.C. Shi designed the toolbox for data processing; F. Liu grew the samples with the guidance of X.Q. Wang; T. Wang prepared the TEM sample; R.C. Shi, B. Sun, S.S. Sheng, B. Shen and W.K. Ge helped with data interpretation. H.L. Jiang wrote the manuscript assisted by T. Wang, B.W. Sheng, P. Wang, L.R. Lindsay, and P. Gao under the direction of X.Q. Wang. All the authors contributed to this work through useful discussion and/or comments on the manuscript.

Competing interests

The authors declare no competing interests.

Additional information

Supplementary information The online version contains supplementary material available at <https://doi.org/10.1038/s41467-024-53394-z>.

Correspondence and requests for materials should be addressed to Tao Wang, Lucas Lindsay or Xinqiang Wang.

Peer review information *Nature Communications* thanks the anonymous reviewer(s) for their contribution to the peer review of this work. A peer review file is available.

Reprints and permissions information is available at <http://www.nature.com/reprints>

Publisher's note Springer Nature remains neutral with regard to jurisdictional claims in published maps and institutional affiliations.

Open Access This article is licensed under a Creative Commons Attribution-NonCommercial-NoDerivatives 4.0 International License, which permits any non-commercial use, sharing, distribution and reproduction in any medium or format, as long as you give appropriate credit to the original author(s) and the source, provide a link to the Creative Commons licence, and indicate if you modified the licensed material. You do not have permission under this licence to share adapted material derived from this article or parts of it. The images or other third party material in this article are included in the article's Creative Commons licence, unless indicated otherwise in a credit line to the material. If material is not included in the article's Creative Commons licence and your intended use is not permitted by statutory regulation or exceeds the permitted use, you will need to obtain permission directly from the copyright holder. To view a copy of this licence, visit <http://creativecommons.org/licenses/by-nc-nd/4.0/>.

© The Author(s) 2024